Low-dose 4D-STEM Tomography for Beam-Sensitive Nanocomposites

Milena Hugenschmidt[1], Daen Jannis[1], Ajinkya Anil Kadu[1,2], Lukas Grünewald[1], Sarah De Marchi[3,4], Jorge Pérez-Juste[3,4], Johan Verbeeck[1], Sandra Van Aert[1,], Sara Bals[1,*]*

[1] EMAT and NanoLab, University of Antwerp, Groenenborgerlaan 171, Antwerp, 2020, Belgium

[2] Centrum Wiskunde & Informatica, Science Park 123, 1098 XG Amsterdam, The Netherlands

[3] CINBIO, Universidade de Vigo, Departamento de Química Física, Campus Universitario As Lagoas, Marcosende, 36310 Vigo, Spain

[4] Galicia Sur Health Research Institute (IIS Galicia Sur), SERGAS-UVIGO, 36310 Vigo, Spain

Email Address: Sandra.VanAert@uantwerpen.be; Sara.Bals@uantwerpen.be

ORCIDs:

MH: 0000-0001-5020-9302
DJ: 0000-0003-0285-0511
AAK: 0000-0003-0853-1378
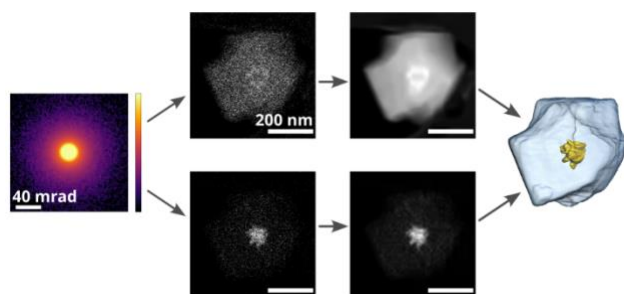LG: 0000-0002-5898-0713
SDM: 0000-0003-0536-8237
JPJ: 0000-0002-4614-1699
JV: 0000-0002-7151-8101
SVA: 0000-0001-9603-8764
SB: 0000-0002-4249-8017

For Table of Contents Only

Abstract

Electron tomography is essential for investigating the three-dimensional (3D) structure of nanomaterials. However, many of these materials, such as metal-organic frameworks (MOFs), are extremely sensitive to electron radiation, making it difficult to acquire a series of projection images for electron tomography without inducing electron-beam damage. Another significant challenge is the high contrast in high-angle annular dark field scanning transmission electron microscopy that can be expected for nanocomposites composed of a metal nanoparticle and a MOF. This strong contrast leads to so-called metal artifacts in the 3D reconstruction. To overcome these limitations, we here present low-dose electron tomography based on four-dimensional scanning transmission electron microscopy (4D-STEM) datasets, collected using an ultrafast and highly sensitive direct electron detector. As a proof of concept, we demonstrate the applicability of the method for an Au nanostar embedded in a ZIF-8 MOF, being of great interest for applications in various fields, including drug delivery.

Due to their hybrid nature, nanocomposites consisting of a metal-organic framework (MOF) and a metal nanoparticle (NP)[1] are of great interest for applications in various fields including drug delivery,[2–4] catalysis,[5] and chemical sensing.[6] In this work, we focus on a composite consisting of a plasmonic, star-shaped nanoparticle embedded in a shell of a ZIF-8 MOF.[7,8] This nanocomposite is envisioned to serve in the light-triggered release of substances inside living cells, or as nanoreactors for specific reactions inside organisms.[2,3] The three-dimensional (3D) structure strongly influences the nanocomposites' properties: the MOF must tightly enclose the metallic core, and the NP shape is essential as it controls its plasmonic properties.[9] Techniques such as (*in vivo*) confocal optical microscopy, surface-enhanced Raman spectroscopy, and SEM are used to characterize the loading and leaking of drugs into/from the MOF, as well as to study morphology and behavior in living cells.[2,3] However, (3D) information concerning the nanocomposite stability is still lacking on a local level.

Scanning transmission electron microscopy (STEM) is a high-resolution imaging technique that can provide structural information about nanocomposites even on the (sub-) nanometer scale. The image is generated by scanning an electron-transparent sample with a focused electron beam and collecting the transmitted electrons below the sample. Most commonly a ring-shaped or radially segmented annular detector, which integrates the signal of electrons for different scattering angles, is used as a detector.[10] The technique inherently produces two-dimensional (2D) projection images, which may disguise the 3D morphology of the imaged material. 3D characterization techniques such as electron tomography (ET) overcome this restriction by reconstructing a 3D volume, based on a series of 2D images that are acquired at different tilt angles, over a range of typically $\pm 70°$ to $80°$.[11–13] These images are then processed by (iterative) back-projection techniques to reconstruct the 3D volume.[14]

One important issue when applying ET is the often significant accumulation of electron dose and therefore beam damage during the serial imaging, resulting in a transformed nanostructure that obstructs a trustworthy 3D reconstruction.[12,15,16] The relevance of this problem is even increased for MOFs that are particularly sensitive to electron radiation and which lose their crystallinity already at an accumulated dose of 5-30 electrons/$Å^2$.[17–19] This amorphization process is often accompanied by a change in the morphology of MOF particles, particularly shrinkage.[14,19,20] Whereas amorphization is not an issue for non-atomically resolved tomography, shrinkage is synonymous with a change in the volume, which is not acceptable during tomogram acquisition. Various solutions to reduce the accumulated dose during serial imaging and thus mitigating beam damage have been proposed in the past, but often one has to accept a certain degree of change in the investigated particle.[12,21] However, especially when several 3D reconstructions are to be performed on one particle, for example, to investigate transformations as a result of *in situ* triggers, shrinkage of the sample by the electron beam is not acceptable.[9]

An additional challenge for ET applied to MOF-metal nanocomposites is the different scattering power of the materials. Whereas MOFs are built from mostly light atoms and thus not strongly scattering, the metal is dense and strongly scattering. In high-angle annular dark-field (HAADF) STEM imaging, where the flexibility of the choice in detection angles is limited, the metal usually has a high intensity compared to the MOF, leading to a strong contrast between the two materials. In the reconstruction, this can lead to a so-called metal artifact with incorrectly low intensities around the metal, which in general usually appears when there is a highly scattering material inside a less scattering matrix. [22–24] Currently, metal artifacts are either reduced by a

careful selection of camera lengths and STEM detector segments or different post-processing techniques.[22–24]

In recent years, four-dimensional scanning transmission electron microscopy (4D-STEM), where a convergent electron beam is scanned over a sample while a diffraction pattern is recorded below the sample at each scan point, has been recognized to be a viable technique for low-dose imaging of beam-sensitive and weakly scattering materials.[25–28] In particular, event-based pixelated direct electron detectors can detect single electrons with a time resolution of 1.56 ns. This enables the full recording of 4D-STEM datasets at microsecond dwell times which are standard in more conventional STEM methods using annular detectors.[29,30]

Here, we employ 4D-STEM datasets to generate virtual STEM (vSTEM) images by integrating specific scattering angles from the diffraction patterns.[31] After repeating this process for acquisitions along different tilt angles, we thus generate ET tilt series based on 4D-STEM, making use of the flexibility in selecting detected scattering angles for the vSTEM images that simultaneously optimize the contrast for weakly and highly scattering angles. More specifically, the detection angles are chosen in such a manner that for every 4D-STEM dataset, two vSTEM images are generated, one of which mainly yields information on the MOF, and the other one represents the NP, which allows mitigating the metal artifact by a separate reconstruction. Attention must be paid to the fulfillment of the so-called projection requirement for electron tomography stating that the signal in the vSTEM images has to be an ideally linear, but at least monotonic function of the imaged object's thickness.[10] Further details on this can be found in the Supporting Information (SI).

We show the application of 4D-STEM tomography to Au nanostars embedded in ZIF-8 (denoted as Au nanostars@ZIF-8). The extreme beam sensitivity of ZIF-8 in STEM imaging has prevented damage-free tomograms in the past, as the material is prone to amorphization and shrinkage under the electron beam. The main advantage of the 4D-STEM tomography technique is that due to the single-electron counting ability of the camera, the dose can be considerably lower than when using a conventional STEM detector, such that shrinkage of the MOF is largely prevented. This approach is not limited to NP@MOF composites only but might find wide application in the 3D investigations of other beam-sensitive materials.

A tilt series was recorded with 10° increments from -70° to +70° with a 4D-STEM scan of 512 × 512 px (2.16 nm/px) in real space and 256 × 256 px in diffraction space (on a Timepix3 camera) at each tilt step. Despite the introduction of golden ratio scanning (GRS) in recent studies, we opted for sequential scanning due to the practical limitations of GRS in our 4D-STEM mode, particularly the challenges in real-time adjustments during tilt-series acquisition.[21]

Notably, the large pixel size of 2.16 nm reduced the areal dose when compared to atomically resolved images. The camera length was chosen to be relatively short (46 mm) to cover higher angles with the camera (0 – 134 mrad up to the diagonal maximum). The convergence angle of the beam was set to 13.43 mrad, to increase the depth of focus and reduce the size of the zero-order beam on the camera.

The pixel size is sufficient to resolve the 3D morphology of the nanocomposite. With a beam current of approximately 1 pA at 300 keV and a recording dwell time of 2 µs, this results in an

estimated incoming dose of 0.03 e$^-$/Å^2 per scan. This results in approximately 0.4 e$^-$/Å^2 for the full tilt series (15 scans). However, the total dose applied to a given particle will be slightly higher due to the time that is spent adjusting the particle position before the tilt series and centering it during the tilt series. The latter was done through one (or sometimes more) additional scan(s) at a short dwell time and lower magnification to minimize the dose. Focusing was done using the Ronchigram from the carbon support close to the particle, preventing sample damage induced to the MOF-nanoparticle composite in this step. Even with a total dose that is up to 2-3 times higher, due to the centering of the particle, the tilt series can be considered an extremely low-dose experiment, compared to typical total doses in the range of 10-10^4 e$^-$/Å^2 for what is generally considered to be a low electron dose in materials sciences.[15,32]

The first post-processing step is identifying suitable angular ranges to generate vSTEM images with sufficient signal for the MOF and the NP, respectively. The camera covers angles between 0 and approximately 134 mrad, allowing to generate bright- or annular-dark field (ADF) vSTEM images. To investigate if there is dominant scattering from the MOF or the NP into specific scattering angular ranges, the location of the MOF and the NP first needs to be identified in the real-space images. Therefore, a vSTEM image is generated by integrating the counts detected over a range of 52 to 90 mrad (**Figure 1**a). The resulting image is thresholded to mask the parts showing the MOF and the NP, respectively (Figure 1b). Integrating the diffraction patterns from the masked area yields position-averaged convergent-beam electron diffraction (PACBED) patterns as shown next to the masks. Notably, the central disk (the zero-order beam) is more intense in the MOF area, whereas the intensities seem more distributed in the NP area, which can be understood by the stronger scattering power of the NP. For a direct comparison, the intensities in the pattern need to be azimuthally integrated and normalized with the intensity of the central disk (**Figure 2a**). This figure shows that the intensity of the MOF signal decreases quickly as a function of the scattering angle, whereas the NP still yields a significant signal above 60 mrad. This analysis enables us to determine integration angles that will result in a dominating signal of the MOF or the NP in the vSTEM images. For the MOF, low scattering angles between 19 and 34 mrad (marked in Figure 2a) appear appropriate. Notably, the signal from the NP in this area is not zero. This means that the vSTEM images generated with these scattering angles will still yield signal from the NP. However, since the MOF signal is significant and does not fall short of the NP intensity by a multiple, we do not expect the reconstruction to be distorted, e.g., by a metal artifact. Depending on the scattering power and the maximum thickness of the observed material, attention has to be paid to not selecting small angles where the signal would no longer linearly depend on thickness, as

described in the next section. For the NP, a higher and broader range of scattering angles (52 - 90 mrad) is expected to yield a good signal with negligible contribution from the MOF shell.
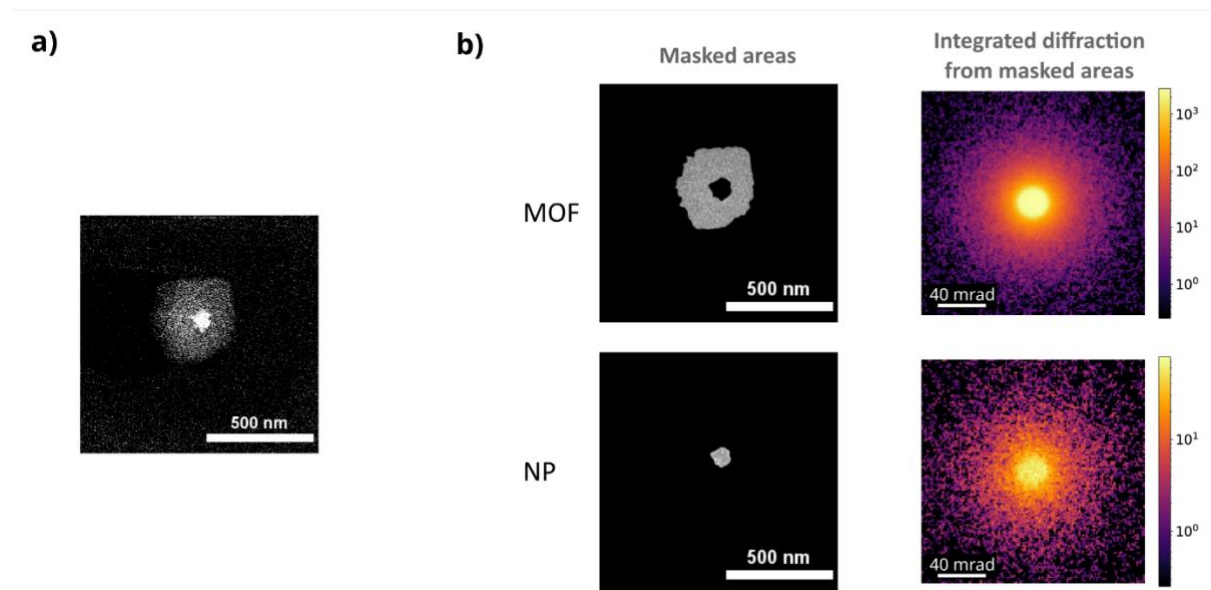

Figure 1: **a)** vSTEM image of the NP@ZIF-8 composite at 20° tilt angle. **b)** Masked areas of the image in (a) and the integrated diffraction patterns from the MOF area (top) and the NP area (bottom), shown on a logarithmic scale and binned with factor 2.
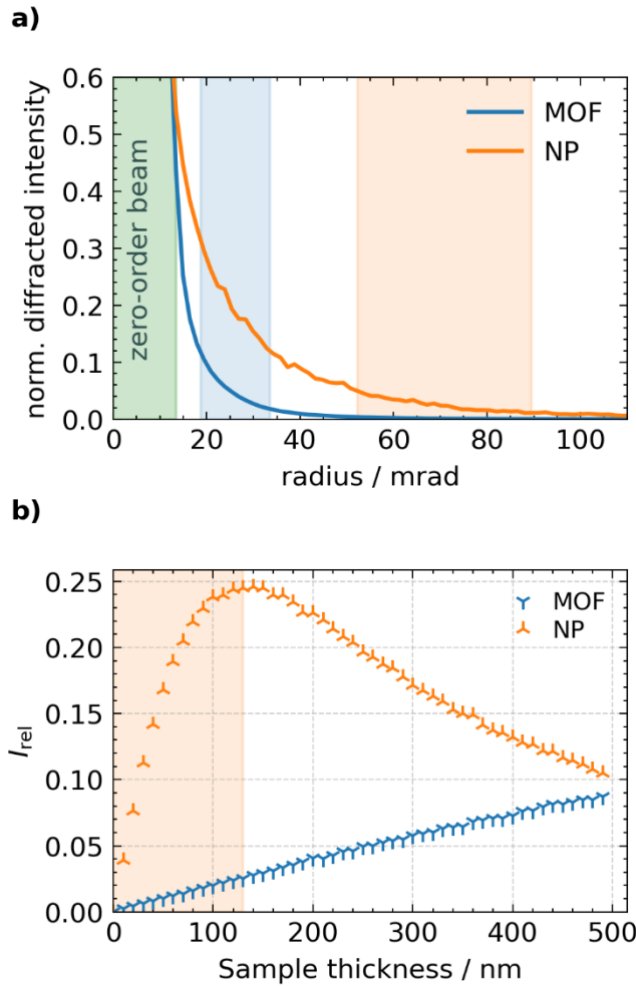
Figure 2: **a)** Azimuthally integrated scattered intensities from the position-averaged diffraction patterns from the MOF and the NP based on the 4D-STEM dataset as a function of the radius of the diffraction pattern in mrad. The intensities are normalized with the intensity of the zero-order beam. The radius of the zero-order beam, as well as two angle ranges that are considered to obtain a distinct signal for the MOF and the NP, respectively, are marked. **b)** Simulated relative scattered intensity I_{rel} at 300 keV for the MOF ZIF-8 and the Au NP, integrated for scattering angles from 19 to 34 mrad for the MOF and 52 to 90 mrad for the NP, as a function of sample thickness.

Given the likely lost or strongly alternated crystallinity of the MOF while collecting the tomography dataset, a Monte Carlo electron-trajectory simulation rather than a multislice simulation has been carried out to test the projection requirement for the MOF and the NP, namely a monotonic, ideally linear dependence of the MOF scattering intensity on the sample thickness for the evaluated scattering angles. In a Monte Carlo simulation, an incident electron penetrates the sample and freely propagates before being scattered elastically or inelastically. At such scattering events, the electron is deflected by a scattering angle θ. This process repeats until the electron leaves the sample or is stopped/absorbed due to significant energy losses. To calculate a statistically relevant result of the fraction of incident electrons leaving the sample under a specific net scattering angle, thousands of electrons have to be simulated, corresponding to a stationary probe on the sample.[33,34] Such a Monte Carlo simulation includes the dependency of composition and density of the material whereas the wave properties of the electron beam, and hence diffraction contrast, are neglected.[17–19]

For the MOF, the latter is viable since ZIF-8 is quickly amorphized under electron irradiation and thus the contribution of crystallinity can likely be neglected.[18] This is confirmed experimentally since the vSTEM tilt series generated from the above-mentioned collection angles do not show Bragg diffraction contrast (which would result in varying intensities depending on the tilt angle). For details regarding the simulation, we refer the reader to the experimental section. The simulation shows that the ADF intensity for a virtual detector integrating between 19 and 34 mrad can be used for tomographic reconstruction of the MOF since the intensity is sufficiently linear up to a sample thickness of at least 500 nm (**Figure 2b**), whereas the MOF diameter is around 400 nm.

We assumed a Monte Carlo simulation of this type also to be valid to test the projection requirement for the NP since the projection images of the NP show no Bragg diffraction contrast either. We additionally checked for a possible diffraction contribution to the images with a powder diffraction simulation, which calculates all possible diffraction for a randomly oriented crystal structure as a function of the scattering angle. The simulation indeed showed that no dominant diffraction is to be expected in the angular range that is evaluated for the vSTEM images of Au (SI, **Figure S1**). 4D-STEM tomography hence offers a direct approach to minimize the impacts of Bragg scattering by employing suitable scattering angles for reconstructing the vSTEM images. This aids in resolving the violation of the projection requirement caused by the occurrence of Bragg diffraction.

For the Monte Carlo-simulated relative intensities scattered into angles between 52 and 90 mrad that were evaluated for the Au NP, we find a maximum at 140 nm (Figure 2b). This means that for thicker samples, the projection requirement would not be fulfilled and tomographic reconstruction will no longer be reliable. The Au NP investigated here has a maximum tip-to-tip diameter of around 130 nm, which means that the projection requirement is still fulfilled, although the curve cannot be approximated as linear for the higher thicknesses. For larger NPs, it would be advisable to use a shorter camera length for covering higher scattering angles and pushing the maximum in scattered intensities to higher sample thicknesses.

Extracting vSTEM images using the designated angular ranges corresponding to the MOF (19 - 34 mrad, **Figure 3** a) and the NP (52 - 90 mrad, **Figure 3** b) results in images such as those in **Figure 3** c, d. The images are quite noisy, with a signal of ~ 6 counts/px in Figure 3 c, averaged over the MOF area, and ~10 counts/px in Figure 3 d in the area of the NP, due to the minimized electron dose used for imaging. To improve the signal-to-noise ratio of the resulting images, a denoising algorithm has been applied. Since the total counts in the vSTEM images, as well as the readout noise of the detector, is low, the noise in the images can be considered to be mainly Poisson distributed. The individual images were hence denoised using an "Iterative Poisson image denoising software" that is publicly available as a Matlab implementation.[35,36] The choice of the denoising algorithm is explained in more detail in the SI. The denoising improves the images by enhancing the intensity differences in the MOF shell (Figure 3 e, see arrows) as well as those corresponding to the dendrites of the star-shaped NP (Figure 3 f). For the NP image, less strong denoising was applied to keep a balance between removing all noise and preservation of the dendrites (see Section *Experimental Section*). We expect that the selection of the denoising strength will not have a substantial influence on the subsequent reconstruction, provided that the majority of the noise is eliminated without introducing blur and the algorithm

avoids generating unreal intensity fluctuations, both of which is evident in the images. The denoised image series were used in the following reconstruction.
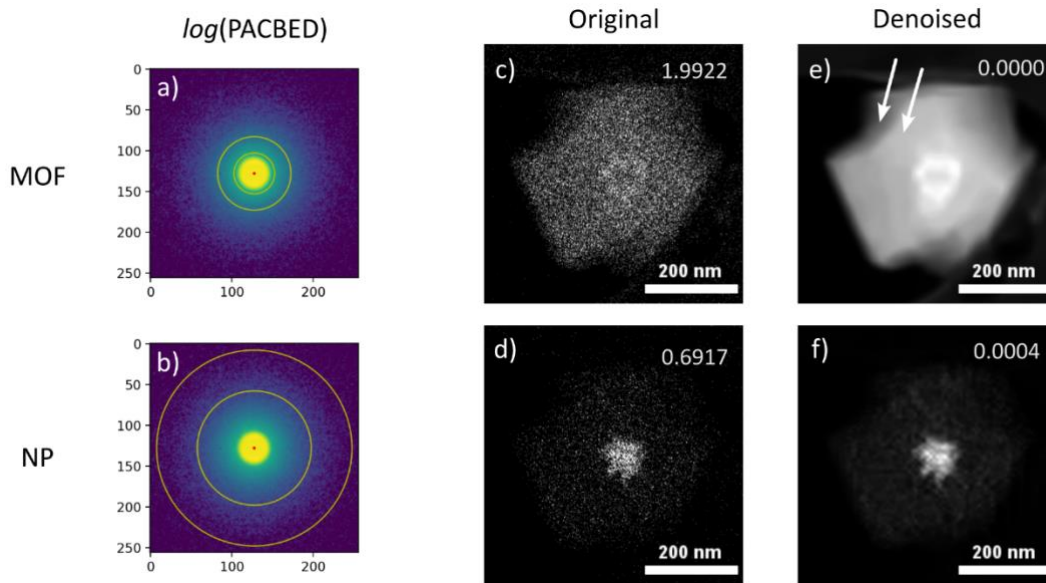

Figure 3: (a,b) The PACBED patterns of the 4D-STEM dataset at -30° sample tilt, with the evaluated angles for MOF and NP marked, (c, d) the corresponding (cropped) vSTEM images, and (e,f) the denoised vSTEM images. The noise levels of the original and denoised vSTEM images are given in their top-right corner.[37]

The denoised, non-masked images (Figure 3 e,f) are used for the 3D reconstruction. The NP will add some contribution to the MOF reconstruction since a residual NP signal is evident in the MOF images (Figure 3 e). Similarly, the remaining signal from the MOF in the NP images will contribute to the NP reconstruction. These unwanted intensity contributions, however, are so low that this is not expected to cause artifacts that will hamper the segmentation of the volumes. The complete denoised tilt series can be found in the SI.

The tomographic reconstruction of the denoised tilt series was performed using the expectation maximization (EM) algorithm for both the MOF and the NP.[38] The optimal number of reconstruction iterations was quantitatively assessed by comparing the denoised vSTEM images with the images produced by forward projections of the reconstructed volume for a range of reconstruction iterations. Calculating the multiscale structural similarity (MS-SSIM) index for image quality for the forward projections and denoised vSTEM images as reference, allows us to quantify the similarity between the experimental images and the result from the reconstruction and thus the reconstruction quality.[39]. An MS-SSIM closer to 1 indicates better and closer to 0 worse reconstruction quality. Averaging the MS-SSIM over the tilt angles for different numbers of reconstruction iterations indicates the optimal number of iterations. Interestingly, beyond a certain number of iterations, the mean MS-SSIM begins to decline, a phenomenon resulting from the EM algorithm fitting noise present in the data.[40] **Figure 4a** shows a maximum mean MS-SSIM and hence an optimal reconstruction for the MOF with 24 iterations, whereas the MS-SSIM for the NP saturates at around 80 iterations. As a result, these numbers of iterations are used in the following.

The MS-SSIM between the tilt series of images and forward projections for the optimal numbers of reconstructions is relatively constant at around 0.95 for absolute tilt angles up to ± 40° and slightly decreases at higher tilt angles both for the MOF and the NP reconstruction, reaching 0.75 as the lowest value for -70° in the MOF reconstruction (Figure 4**b**). The reduction in MS-SSIM at elevated tilt angles arises from complexities in electron scattering patterns, which deviate from the assumptions made in the radon transform approximation, leading to discrepancies between the model and the data. In future work, a potential improvement in the MS-SSIM at high tilt angles could be obtained by integrating more sophisticated physics, such as scattering corrections tailored for the high tilt angles, into the forward scattering model. Exemplary orthoslices, forward projections, and a more detailed discussion of the reconstruction quality can be found in the SI (**Figure S2** and **S3**).
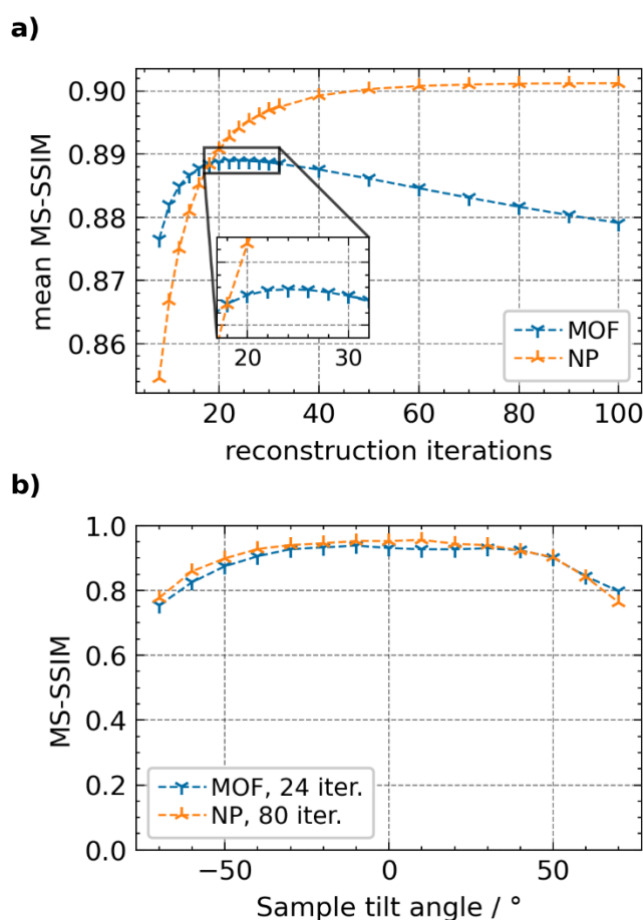

Figure 4: **a)** Mean multiscale structural similarity (MS-SSIM) index between the experimental image series and the forward projections from reconstructions with different numbers of iterations. A value closer to 1 indicates a better reconstruction quality. **b)** MS-SSIM index between the forward projections and the denoised vSTEM images at all tilt angles for the optimum number of iterations.

The shrinkage of the particle after electron tomography was found to be only -0.7%, calculated by evaluating the thresholded projected area of the MOF before and after the image series (**Figure 5a**). This value is within the error margin of around 1%, which is estimated from the precision with which the thresholds for the estimation of the particle area can be set. The shrinkage that is caused in this 4D-STEM tomography series is significantly reduced compared to an optimized fast and low-dose tilt series for conventional STEM tomography that shows a

shrinkage of 5% (**Figure S4**). It is worth noting that the visibility of the NP in Figure 5a is caused by its strong scattering relative to the surrounding MOF complex, which causes capturing some influence of the Au NP in the scattering angles evaluated for the MOF (compare Figure 2a). In addition, the intensity drops in the center of the NP, as the thickness is relatively large there, causing a contrast inversion. However, the NP is a negligible artifact in the MOF images and does not disturb the following segmentation.
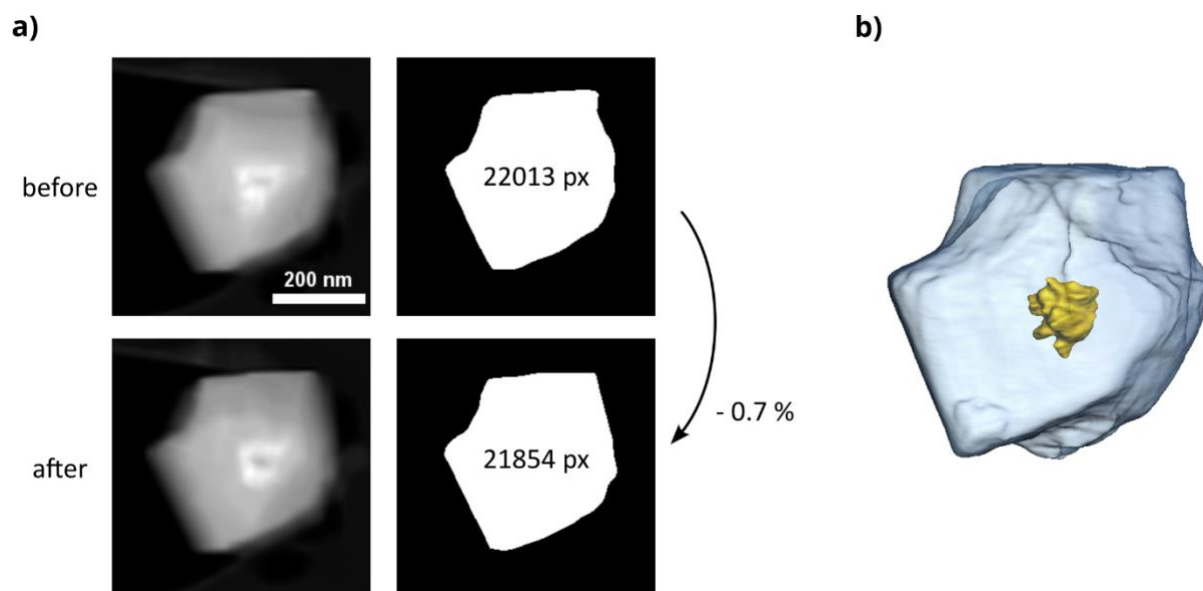

Figure 5: a) Evaluation of the MOF shrinkage during the tilt series by comparing the projected area of the particle at 0° tilt angle before (upper row) and after (lower row) the tilt-series acquisition. b) 3D reconstruction of the MOF and the NP volume.

Despite the artifacts caused by the low image signal and the sparse sampling of the tilt range, the contrast between the volumes is clear. Also, the signal-to-noise ratio in the orthoslices is sufficiently high to segment the volumes of the MOF or the NP, respectively, by simple thresholding using the Amira software. The volume of the MOF and the NP are segmented from their respective volumes and shown together in Figure 5**b**. Both the faceted structure of the initially crystalline MOF and the irregular, star-shaped structure of the NP with its dendrites are resolved. Although the NP is visible in the reconstructed MOF dataset, as shown in Figure S2a, this does not hamper the segmentation of the MOF volume. The segmentation gives information on the MOF-shell thickness, providing insights, e.g., into the thermal insulation ability.[2] We can furthermore conclude that the successful reconstruction of the NP's shape and volume provides us not only information on its size but also on its tip-to-tip lengths, factors that are critical for its tunable plasmonic absorption bands.[2]

Using an electron tomography approach, which employs virtual STEM (vSTEM) images created from 4D-STEM datasets that are recorded at every tilt step of a tomography tilt series, low-dose tomography series with adjustable image contrast can be generated. This is especially advantageous for the 3D investigation of beam-sensitive samples as well as composites, where specific elements yield stronger scattering than others. In this manner, we here demonstrate that shrinkage and metal artifacts can be avoided during electron tomography experiments for nanoparticle-MOF nanocomposites.

Although other methods, such as "fast tomography" are faster,[32] our approach is more dose-effective and is not limited to the angular ranges offered by a conventional STEM detector. In the future, the time required for a 4D-STEM tomography series, which is now extended by many manual steps, can be drastically shortened by a more user-friendly integration of event-based detectors into the microscope system. Exploring more advanced reconstruction algorithms that can better handle sparse tilt steps and can potentially lead to reconstructions of better quality. Due to the dose-efficiency of our 4D-STEM tomography approach, we envision it as useful for *in situ* studies of MOFs and other beam-sensitive materials, which are not possible without mitigating irradiation damage leading to sample shrinkage. In the future, this may include high-resolution, low-dose STEM tomography.

Experimental Section

Synthesis of Au nanostars. Au nanostars were synthesized following a previously reported seed-mediated growth method with some modifications.[41] Briefly, 0.9 mL of solution of citrate stabilized gold seeds (ca. 15 nm in diameter, [Au] = 0.5 mM), prepared by the Turkevich method,[42] were added to 90 mL of a growth solution containing $HAuCl_4$ (0.25 mM) and HCl (1 mM, 90 μL), followed by simultaneous addition of $AgNO_3$ (2 mM, 0.9 mL) and ascorbic acid (100 mM, 0.45 mL) under vigorous stirring. Then, after 5 min, 1.44 mL of a 0.75 M solution of CTAC was added to the Au nanostars dispersion. Finally, the solution was centrifuged (4000 rpm, 20 min) twice to remove excess reactants, and redispersed in aqueous CTAC solution ([CTAC]= 0.6 mM and [Au]= 2.4 mM).

ZIF-8 encapsulation. The individual encapsulation of Au nanostars within ZIF-8 nanocrystals was based on a previously reported protocol with some modifications.[8] Typically, 0.144 mL of CTAB (1 mM) was added to 1 mL of an aqueous solution of 2-methylimidazole (1.32 M). The solution was stirred for 5 min and then 1 mL of aqueous Zn $(NO_3)_2 \cdot 6H_2O$ (24 mM) and 1 mL of Au stars were sequentially added under vigorous stirring. After 5 min of further magnetic stirring, the solution was left undisturbed for 3 h. The resulting core-shell NS@ZIF-8 nanoparticles were centrifuged twice (5000 rpm, 10 min) to remove the excess reactants and free ZIF-8 nanocrystals. The resulting pellets were resuspended first in 10 mL of methanol and finally in 3.14 mL of methanol.

Data collection: 4D-STEM datasets were recorded using a probe-corrected Titan Themis Transmission Electron Microscope (Thermo Fisher Scientific, Eindhoven, Nederlands), equipped with a monochromator, using an event-based detector, the AdvaPIX TP3 (camera module with Timepix3 readout chip).[43] A camera length of 46 mm was set to cover higher diffraction angles with the Timepix3 detector. At this camera length, 1 pixel on the camera corresponds to 0.746 mrad in diffraction space. The used electron current of 1 pA (Spot size 11, C2 Aperture 50 μm, Monochromator focus 270 eV from cross-over) was calculated, according to Jannis *et al.,* from the counts per minute measured on the Timepix3 with an estimated cluster size of 3 px.[29] The low dose results in an average of approximately 40 counts per diffraction pattern in the 4D-STEM datasets, which equals an average of 0.002 counts per pixel of the camera, including the zero-order beam.

Simulations: The relative scattered intensities as a function of thickness for ZIF-8 and Au were simulated with a Monte Carlo approach using the NISTMonte1.2 software package.[44] In this, scattering was described by the Screened Rutherford Cross-Section and the energy loss of electrons by the continuous-slowing-down approximation.[10] 100.000 electron trajectories were simulated. For ZIF-8, the sample was defined by the molar fraction of the elements in ZIF-8 ($C_{24}H_{30}N_{12}O_{10}Zn_3$),[45] and a material density of 0.95 g/cm^3.[46] For the NP, pure Au with a density of 19.3 g/cm^3 was assumed. The powder diffraction intensities for Au were simulated using the scikit-ued (2.1.13) and Crystals (1.6.2) Python packages.[47]

Data evaluation: The electron beam current has been estimated from 19500 counts/ms on the detector without a sample and a cluster size of 3 (number of pixels excited by one electron) that was estimated based on the characterizations by Jannis et al.[29] Generation of 4D-STEM datacubes and vSTEM images was done using a toolset by Jannis *et al.*[29,48] Masking of the hdf5 dataset for the inspection of signals was done similarly to a workflow by Grünewald,[49] using HyperSpy 1.7.3.[50] The dimensions on the camera have been calibrated by comparing the known

convergence angle with its diameter on the camera. Image denoising using the iterative Poisson image denoising software that applies variance stabilizing transformations for standardizing the noise and BM3D Gaussian denoising filtering.[35,36] The MOF images were multiplied by 0.15 before applying the filter; the NP images by 0.6. A smaller value leads to stronger denoising.

The Astra Toolbox 1.9.0,[38,51] extended with some in-house functions, was used for the reconstruction of the volumes, employing the EM algorithm. The Fiji/ImageJ toolbox was used to inspect the orthoslices,[52] while the segmentation and 3D representation were prepared with the commercial Amira 5.4.0 software by Thermo Fisher Scientific.

For the graphics, we used the matplotlib graphics package for Python (3.6.2),[53] the scienceplots library (2.0.1),[54] and Inkscape 1.2. The Fiji toolset em-scalebartools 0.3.2 was used for scale bar formatting.[55]

Supporting Information. Description of the projection requirement, discussion of the denoising algorithm and the reconstruction quality, low-resolution TEM images of the NP@ZIF-8 composite as well as UV-vis spectra of the NP and the composite, and tilt series of the MOF and the NP (original and denoised). A video of the 3D volume is provided as separate file.

Credit author statement

Milena Hugenschmidt – Conceptualization, Methodology, Software, Data Curation, Investigation, Writing - Original Draft, Writing - Review & Editing, Visualization

Daen Jannis – Software, Data Curation

Ajinkya Anil Kadu – Software, Writing - Review & Editing

Lukas Grünewald – Software, Data Curation, Writing - Review & Editing

Sarah De Marchi – Resources, Writing - Review & Editing

Jorge Pérez-Juste – Supervision, Writing - Review & Editing

Johan Verbeeck – Supervision, Writing - Review & Editing

Sandra Van Aert – Conceptualization, Writing - Review & Editing, Supervision

Sara Bals – Conceptualization, Writing - Review & Editing, Supervision, Project administration, Funding acquisition

Acknowledgments

Data Availability

Data for this publication and evaluation documentation is openly available in a public repository at doi.org/10.5281/zenodo.8042880.[56]

References

(1) Yaghi, O. M.; Li, G.; Li, H. Selective Binding and Removal of Guests in a Microporous Metal–Organic Framework. *Nature* **1995**, *378*, 703–706. https://doi.org/10.1038/378703a0.

(2) Carrillo-Carrión, C.; Martínez, R.; Polo, E.; Tomás-Gamasa, M.; Destito, P.; Ceballos, M.; Pelaz, B.; López, F.; Mascareñas, J. L.; Pino, P. del. Plasmonic-Assisted Thermocyclizations in Living Cells Using Metal–Organic Framework Based Nanoreactors. *ACS Nano* **2021**, *15*, 16924–16933. https://doi.org/10.1021/acsnano.1c07983.

(3) Carrillo-Carrión, C.; Martínez, R.; Navarro Poupard, M. F.; Pelaz, B.; Polo, E.; Arenas-Vivo, A.; Olgiati, A.; Taboada, P.; Soliman, M. G.; Catalán, Ú.; Fernández-Castillejo, S.; Solà, R.; Parak, W. J.; Horcajada, P.; Alvarez-Puebla, R. A.; del Pino, P. Aqueous Stable Gold Nanostar/ZIF-8 Nanocomposites for Light-Triggered Release of Active Cargo Inside Living Cells. *Angewandte Chemie International Edition* **2019**, *58*, 7078–7082. https://doi.org/10.1002/anie.201902817.

(4) Martínez, R.; Carrillo-Carrión, C.; Destito, P.; Alvarez, A.; Tomás-Gamasa, M.; Pelaz, B.; Lopez, F.; Mascareñas, J. L.; del Pino, P. Core-Shell Palladium/MOF Platforms as Diffusion-Controlled Nanoreactors in Living Cells and Tissue Models. *Cell Reports Physical Science* **2020**, *1*, 100076. https://doi.org/10.1016/j.xcrp.2020.100076.

(5) Kuo, C.-H.; Tang, Y.; Chou, L.-Y.; Sneed, B. T.; Brodsky, C. N.; Zhao, Z.; Tsung, C.-K. Yolk–Shell Nanocrystal@ZIF-8 Nanostructures for Gas-Phase Heterogeneous Catalysis with Selectivity Control. *J. Am. Chem. Soc.* **2012**, *134*, 14345–14348. https://doi.org/10.1021/ja306869j.

(6)   Sugikawa, K.; Nagata, S.; Furukawa, Y.; Kokado, K.; Sada, K. Stable and Functional Gold Nanorod Composites with a Metal–Organic Framework Crystalline Shell. *Chem. Mater.* **2013**, *25*, 2565–2570. https://doi.org/10.1021/cm302735b.

(7)   Park, K. S.; Ni, Z.; Côté, A. P.; Choi, J. Y.; Huang, R.; Uribe-Romo, F. J.; Chae, H. K.; O'Keeffe, M.; Yaghi, O. M. Exceptional Chemical and Thermal Stability of Zeolitic Imidazolate Frameworks. *Proceedings of the National Academy of Sciences* **2006**, *103*, 10186–10191. https://doi.org/10.1073/pnas.0602439103.

(8)   Zheng, G.; de Marchi, S.; López-Puente, V.; Sentosun, K.; Polavarapu, L.; Pérez-Juste, I.; Hill, E. H.; Bals, S.; Liz-Marzán, L. M.; Pastoriza-Santos, I.; Pérez-Juste, J. Encapsulation of Single Plasmonic Nanoparticles within ZIF-8 and SERS Analysis of the MOF Flexibility. *Small* **2016**, *12*, 3935–3943. https://doi.org/10.1002/smll.201600947.

(9)   Vanrompay, H.; Bladt, E.; Albrecht, W.; Béché, A.; Zakhozheva, M.; Sánchez-Iglesias, A.; Liz-Marzán, L. M.; Bals, S. 3D Characterization of Heat-Induced Morphological Changes of Au Nanostars by Fast in Situ Electron Tomography. *Nanoscale* **2018**, *10*, 22792–22801. https://doi.org/10.1039/C8NR08376B.

(10)   *Springer Handbook of Microscopy*; Hawkes, P. W., Spence, J. C. H., Eds.; Springer Handbooks; Springer International Publishing: Cham, 2019. https://doi.org/10.1007/978-3-030-00069-1.

(11)   Kübel, C.; Voigt, A.; Schoenmakers, R.; Otten, M.; Su, D.; Lee, T.-C.; Carlsson, A.; Bradley, J. Recent Advances in Electron Tomography: TEM and HAADF-STEM Tomography for Materials Science and Semiconductor Applications. *Microscopy and Microanalysis* **2005**, *11*, 378–400. https://doi.org/10.1017/S1431927605050361.

(12) Jenkinson, K.; Liz-Marzán, L. M.; Bals, S. Multimode Electron Tomography Sheds Light on Synthesis, Structure, and Properties of Complex Metal-Based Nanoparticles. *Advanced Materials* **2022**, *34*, 2110394. https://doi.org/10.1002/adma.202110394.

(13) Angelomé, P. C.; Heidari Mezerji, H.; Goris, B.; Pastoriza-Santos, I.; Pérez-Juste, J.; Bals, S.; Liz-Marzán, L. M. Seedless Synthesis of Single Crystalline Au Nanoparticles with Unusual Shapes and Tunable LSPR in the Near-IR. *Chem. Mater.* **2012**, *24*, 1393–1399. https://doi.org/10.1021/cm3004479.

(14) *Electron Tomography: Methods for Three-Dimensional Visualization of Structures in the Cell*, 2nd ed.; Frank, J., Ed.; Springer: New York ; London, 2006.

(15) Esteban, D. A.; Vanrompay, H.; Skorikov, A.; Béché, A.; Verbeeck, J.; Freitag, B.; Bals, S. Fast Electron Low Dose Tomography for Beam Sensitive Materials. *Microscopy and Microanalysis* **2021**, *27*, 2116–2118. https://doi.org/10.1017/S1431927621007649.

(16) Albrecht, W.; Bals, S. Fast Electron Tomography for Nanomaterials. *J. Phys. Chem. C* **2020**, *124*, 27276–27286. https://doi.org/10.1021/acs.jpcc.0c08939.

(17) Zhang, D.; Zhu, Y.; Liu, L.; Ying, X.; Hsiung, C.-E.; Sougrat, R.; Li, K.; Han, Y. Atomic-Resolution Transmission Electron Microscopy of Electron Beam–Sensitive Crystalline Materials. *Science* **2018**, *359*, 675–679. https://doi.org/10.1126/science.aao0865.

(18) Zhu, Y.; Ciston, J.; Zheng, B.; Miao, X.; Czarnik, C.; Pan, Y.; Sougrat, R.; Lai, Z.; Hsiung, C.-E.; Yao, K.; Pinnau, I.; Pan, M.; Han, Y. Unravelling Surface and Interfacial Structures of a Metal–Organic Framework by Transmission Electron Microscopy. *Nature Mater* **2017**, *16*, 532–536. https://doi.org/10.1038/nmat4852.

(19) Liu, L.; Zhang, D.; Zhu, Y.; Han, Y. Bulk and Local Structures of Metal–Organic Frameworks Unravelled by High-Resolution Electron Microscopy. *Commun Chem* **2020**, *3*, 1–14. https://doi.org/10.1038/s42004-020-00361-6.

(20) Ghosh, S.; Yun, H.; Kumar, P.; Conrad, S.; Tsapatsis, M.; Mkhoyan, K. A. Two Distinct Stages of Structural Modification of ZIF-L MOF under Electron-Beam Irradiation. *Chem. Mater.* **2021**, *33*, 5681–5689. https://doi.org/10.1021/acs.chemmater.1c01332.

(21) Craig, T. M.; Kadu, A. A.; Batenburg, K. J.; Bals, S. Real-Time Tilt Undersampling Optimization during Electron Tomography of Beam Sensitive Samples Using Golden Ratio Scanning and RECAST3D. *Nanoscale* **2023**, No. 11, 5391–5402. https://doi.org/10.1039/D2NR07198C.

(22) Sentosun, K.; Sanz Ortiz, M. N.; Batenburg, K. J.; Liz-Marzán, L. M.; Bals, S. Combination of HAADF-STEM and ADF-STEM Tomography for Core–Shell Hybrid Materials. *Particle & Particle Systems Characterization* **2015**, *32*, 1063–1067. https://doi.org/10.1002/ppsc.201500097.

(23) Nawaz, S.; Fu, J.; Fan, D. Metal Artifacts Reduction in X-Ray CT Based on Segmentation and Forward-Projection. *Bio-Medical Materials and Engineering* **2014**, *24*, 3287–3293. https://doi.org/10.3233/BME-141151.

(24) Lemmens, C.; Faul, D.; Nuyts, J. Suppression of Metal Artifacts in CT Using a Reconstruction Procedure That Combines MAP and Projection Completion. *IEEE Transactions on Medical Imaging* **2009**, *28*, 250–260. https://doi.org/10.1109/TMI.2008.929103.

(25) Bustillo, K. C.; Zeltmann, S. E.; Chen, M.; Donohue, J.; Ciston, J.; Ophus, C.; Minor, A. M. 4D-STEM of Beam-Sensitive Materials. *Acc. Chem. Res.* **2021**, *54*, 2543–2551. https://doi.org/10.1021/acs.accounts.1c00073.

(26) Lee, J.; Lee, M.; Park, Y.; Ophus, C.; Yang, Y. Multislice Electron Tomography Using 4D-STEM. arXiv October 23, 2022. https://doi.org/10.48550/arXiv.2210.12636.

(27) Zhang, H.; Li, G.; Zhang, J.; Zhang, D.; Chen, Z.; Liu, X.; Guo, P.; Zhu, Y.; Chen, C.; Liu, L.; Guo, X.; Han, Y. Three-Dimensional Inhomogeneity of Zeolite Structure and

Composition Revealed by Electron Ptychography. *Science* **2023**, *380*, 633–638. https://doi.org/10.1126/science.adg3183.

(28) Li, G.; Zhang, H.; Han, Y. 4D-STEM Ptychography for Electron-Beam-Sensitive Materials. *ACS Cent. Sci.* **2022**, *8*, 1579–1588. https://doi.org/10.1021/acscentsci.2c01137.

(29) Jannis, D.; Hofer, C.; Gao, C.; Xie, X.; Béché, A.; Pennycook, T. J.; Verbeeck, J. Event Driven 4D STEM Acquisition with a Timepix3 Detector: Microsecond Dwell Time and Faster Scans for High Precision and Low Dose Applications. *Ultramicroscopy* **2022**, *233*, 113423. https://doi.org/10.1016/j.ultramic.2021.113423.

(30) Auad, Y.; Walls, M.; Blazit, J.-D.; Stéphan, O.; Tizei, L. H. G.; Kociak, M.; De la Peña, F.; Tencé, M. Event-Based Hyperspectral EELS: Towards Nanosecond Temporal Resolution. *Ultramicroscopy* **2022**, *239*, 113539. https://doi.org/10.1016/j.ultramic.2022.113539.

(31) Ophus, C. Four-Dimensional Scanning Transmission Electron Microscopy (4D-STEM): From Scanning Nanodiffraction to Ptychography and Beyond. *Microscopy and Microanalysis* **2019**, *25*, 563–582. https://doi.org/10.1017/S1431927619000497.

(32) Vanrompay, H.; Skorikov, A.; Bladt, E.; Béché, A.; Freitag, B.; Verbeeck, J.; Bals, S. Fast versus Conventional HAADF-STEM Tomography of Nanoparticles: Advantages and Challenges. *Ultramicroscopy* **2021**, *221*, 113191. https://doi.org/10.1016/j.ultramic.2020.113191.

(33) Sousa, A. A.; Hohmann-Marriott, M. F.; Zhang, G.; Leapman, R. D. Monte Carlo Electron-Trajectory Simulations in Bright-Field and Dark-Field STEM: Implications for Tomography of Thick Biological Sections. *Ultramicroscopy* **2009**, *109*, 213–221. https://doi.org/10.1016/j.ultramic.2008.10.005.

(34) Sousa, A. A.; Azari, A. A.; Zhang, G.; Leapman, R. D. Dual-Axis Electron Tomography of Biological Specimens: Extending the Limits of Specimen Thickness with Bright-Field STEM Imaging. *Journal of Structural Biology* **2011**, *174*, 107–114. https://doi.org/10.1016/j.jsb.2010.10.017.

(35) Azzari, L.; Foi, A. Variance Stabilization for Noisy+Estimate Combination in Iterative Poisson Denoising. *IEEE Signal Processing Letters* **2016**, *23*, 1086–1090. https://doi.org/10.1109/LSP.2016.2580600.

(36) Azzari, L.; Foi, A. *Iterative Poisson image denoising software for Matlab (ver. 7 or later)*. https://webpages.tuni.fi/foi/invansc/.

(37) Liu, X.; Tanaka, M.; Okutomi, M. Single-Image Noise Level Estimation for Blind Denoising. *IEEE Transactions on Image Processing* **2013**, *22*, 5226–5237. https://doi.org/10.1109/TIP.2013.2283400.

(38) van Aarle, W.; Palenstijn, W. J.; De Beenhouwer, J.; Altantzis, T.; Bals, S.; Batenburg, K. J.; Sijbers, J. The ASTRA Toolbox: A Platform for Advanced Algorithm Development in Electron Tomography. *Ultramicroscopy* **2015**, *157*, 35–47. https://doi.org/10.1016/j.ultramic.2015.05.002.

(39) Wang, Z.; Simoncelli, E. P.; Bovik, A. C. Multiscale Structural Similarity for Image Quality Assessment. In *The Thrity-Seventh Asilomar Conference on Signals, Systems & Computers, 2003*; 2003; Vol. 2, pp 1398-1402 Vol.2. https://doi.org/10.1109/ACSSC.2003.1292216.

(40) Hansen, P. C.; Saxild-Hansen, M. AIR Tools — A MATLAB Package of Algebraic Iterative Reconstruction Methods. *Journal of Computational and Applied Mathematics* **2012**, *236*, 2167–2178. https://doi.org/10.1016/j.cam.2011.09.039.

(41) Yuan, H.; Khoury, C. G.; Hwang, H.; Wilson, C. M.; Grant, G. A.; Vo-Dinh, T. Gold Nanostars: Surfactant-Free Synthesis, 3D Modelling, and Two-Photon

Photoluminescence Imaging. *Nanotechnology* **2012**, *23*, 075102.

https://doi.org/10.1088/0957-4484/23/7/075102.

(42) Turkevich, J.; Stevenson, P. C.; Hillier, J. A Study of the Nucleation and Growth

Processes in the Synthesis of Colloidal Gold. *Discuss. Faraday Soc.* **1951**, *11*, 55–75.

https://doi.org/10.1039/DF9511100055.

(43) *First Truly Spectral Imaging Camera - AdvaPIX TPX 3*. ADVACAM.

https://advacam.com/camera/advapix-tpx3 (accessed 2023-03-21).

(44) Ritchie, N. W. M. A New Monte Carlo Application for Complex Sample Geometries.

Surface and Interface Analysis **2005**, *37*, 1006–1011. https://doi.org/10.1002/sia.2093.

(45) Park, K. S.; Ni, Z.; Cote, A. P.; Choi, J. Y.; Huang, R.; Uribe-Romo, F. J.; Chae, H. K.;

O'Keeffe, M.; Yaghi, O. M. CCDC 602542: Experimental Crystal Structure

Determination, 2006. https://doi.org/10.5517/CCN6ZVN.

(46) Tan, J. C.; Bennett, T. D.; Cheetham, A. K. Chemical Structure, Network Topology, and

Porosity Effects on the Mechanical Properties of Zeolitic Imidazolate Frameworks.

Proceedings of the National Academy of Sciences of the United States of America **2010**,

107, 9938. https://doi.org/10.1073/pnas.1003205107.

(47) René de Cotret, L. P.; Otto, M. R.; Stern, M. J.; Siwick, B. J. An Open-Source Software

Ecosystem for the Interactive Exploration of Ultrafast Electron Scattering Data. *Adv

Struct Chem Imag* **2018**, *4*, 11. https://doi.org/10.1186/s40679-018-0060-y.

(48) Jannis, D.; Hofer, C.; Gao, C.; Xie, X.; Béché, A.; Pennycook, T. J.; Verbeeck, J. Event

Driven 4D STEM Acquisition with a Timepix3 Detector: Microsecond Dwelltime and

Faster Scans for High Precision and Low Dose Applications, 2021.

https://doi.org/10.5281/zenodo.5068510.

(49) Grünewald, L. Data-Analysis Notebooks for the Thesis "Electron Microscopic Investigation of Superconducting Fe- and Cu-Based Thin Films," 2022. https://doi.org/10.5445/IR/1000144208.

(50) Peña, F. de la; Prestat, E.; Fauske, V. T.; Burdet, P.; Lähnemann, J.; Jokubauskas, P.; Furnival, T.; Nord, M.; Ostasevicius, T.; MacArthur, K. E.; Johnstone, D. N.; Sarahan, M.; Taillon, J.; Aarholt, T.; pquinn-dls; Migunov, V.; Eljarrat, A.; Caron, J.; Francis, C.; Nemoto, T.; Poon, T.; Mazzucco, S.; actions-user; Tappy, N.; Cautaerts, N.; Somnath, S.; Slater, T.; Walls, M.; Winkler, F.; Ånes, H. W. Hyperspy/Hyperspy: Release v1.7.3, 2022. https://doi.org/10.5281/zenodo.7263263.

(51) Van Aarle, W.; Palenstijn, W. J.; Cant, J.; Janssens, E.; Bleichrodt, F.; Dabravolski, A.; De Beenhouwer, J.; Joost Batenburg, K.; Sijbers, J. Fast and Flexible X-Ray Tomography Using the ASTRA Toolbox. *Opt. Express* **2016**, *24*, 25129. https://doi.org/10.1364/OE.24.025129.

(52) Schindelin, J.; Arganda-Carreras, I.; Frise, E.; Kaynig, V.; Longair, M.; Pietzsch, T.; Preibisch, S.; Rueden, C.; Saalfeld, S.; Schmid, B.; others. Fiji: An Open-Source Platform for Biological-Image Analysis. *Nature methods* **2012**, *9*, 676–682.

(53) Hunter, J. D. Matplotlib: A 2D Graphics Environment. *Computing in Science & Engineering* **2007**, *9*, 90–95. https://doi.org/10.1109/MCSE.2007.55.

(54) Garrett, J.; Luis, E.; Peng, H.-H.; Cera, T.; gobinathj; Tian, H.; Keçeci, M.; Iyer, S.; Liu, Y.; cjw. Garrettj403/SciencePlots: SciencePlots (v2.0.1), 2022. https://doi.org/10.5281/zenodo.7394724.

(55) Grünewald, L. Lukmuk/Em-Scalebartools: V0.3.2, 2023. https://doi.org/10.5281/zenodo.7799311.

(56) Hugenschmidt, M.; Jannis, D.; Kadu, A. A.; Grünewald, L.; Marchi, S. D.; Pérez-Juste, J.; Verbeeck, J.; Aert, S. V.; Bals, S. Supplementary Information and Raw Data for

"Low-Dose 4D-STEM Tomography for Beam-Sensitive Nanocomposites," 2023.

https://doi.org/10.5281/zenodo.8042880.

Low-dose 4D-STEM Tomography for Beam-Sensitive Nanocomposites

Milena Hugenschmidt[1], Daen Jannis[1], Ajinkya Anil Kadu[1,2], Lukas Grünewald[1], Sarah De Marchi[3,4], Jorge Pérez-Juste[3,4], Johan Verbeeck[1], Sandra Van Aert[1,*], Sara Bals[1,*]

[1] EMAT and NanoLab, University of Antwerp, Groenenborgerlaan 171, Antwerp, 2020, Belgium

[2] Centrum Wiskunde & Informatica, Science Park 123, 1098 XG Amsterdam, The Netherlands

[3] CINBIO, Universidade de Vigo, Departamento de Química Física, Campus Universitario As Lagoas, Marcosende, 36310 Vigo, Spain

[4] Galicia Sur Health Research Institute (IIS Galicia Sur), SERGAS-UVIGO, 36310 Vigo, Spain

Email Address: Sandra.VanAert@uantwerpen.be; Sara.Bals@uantwerpen.be

Supporting Information
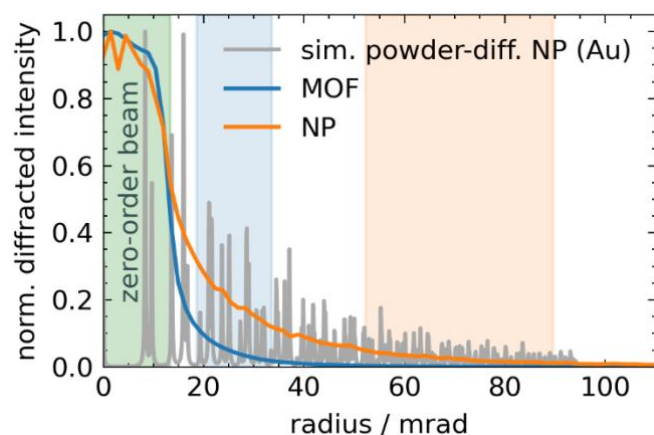
Figure S1: Azimuthally integrated scattered intensities from the position-averaged diffraction patterns from the MOF and the NP based on the 4D-STEM dataset as a function of the radius of the diffraction pattern in mrad, and the integrated simulated powder diffraction pattern for Au.

Projection requirement

Fulfilling the projection requirement is crucial for tomography because it ensures that the image intensity at each point is proportional to the thickness of the sample at that point. The linearity simplifies the reconstruction process as it allows for the direct conversion of the recorded signal into a 3D structure. In practical settings, where achieving ideal linearity can be challenging, a monotonic function serves as a sufficient approximation. This implies that if one part of the sample is thicker than another, it will consistently yield a stronger or weaker signal, depending on the nature of the monotonic function. This consistent trend then still enables the accurate reconstruction of the volume of the imaged object in 3D.

Discussion of the denoising algorithm

Our decision to use the Iterative Poisson image denoising software was based on its proven ability to effectively reduce noise while preserving the important structural details necessary for precise electron tomography reconstructions. It is worth mentioning that the Iterative Poisson denoising algorithm has been recognized for its superior performance in handling images that are corrupted with Poisson noise.[1] Considering the successful application of the Iterative Poisson denoising algorithm in X-ray CT images,[2] the similarity in noise characteristics between X-ray CT images and electron tomographic images adds validity to our denoising process.

Discussion of the reconstruction quality

Exemplary orthoslices through the reconstructed volume in **Figure S2** show a sharp boundary between the volume of interest (either the MOF or the NP) and the dark background. The remaining artifacts in the MOF image are an artificially high intensity outside of the MOF, marked by an arrow, and the residual signal from the NP in the MOF volume, marked with an ellipse (Figure S2a). The first artifact most likely originates from the missing information in the tilt series due to the relatively large steps of 10° in the tilt series. The residual NP signal was already visible in the vSTEM tilt series (see Figure 3e). The grainy structure inside the NP is

another artifact, explained by the remaining noise which is larger here since the images have not been denoised too strongly in a balance to preserve the dendrites of the NP (Figure S1b). The latter would be smeared out by strong denoising.

Again, the quality of the reconstruction can be evaluated by comparing the denoised vSTEM images with the forward projections of the reconstructed volume. **Figure S3** shows this comparison qualitatively for the -30° tilt angle (similar to Figure 3). Although the denoised vSTEM images yield sharper edges in comparison to the forward projections, the general shape of the MOF and even the dendrites of the NP are well reproduced in the forward projections, indicating a high-quality reconstruction.
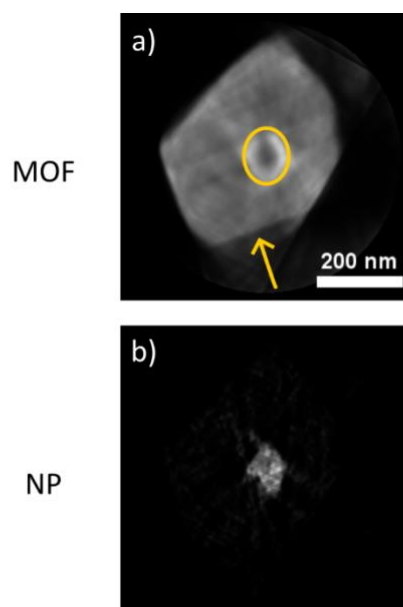
Figure S2: Orthoslices of the reconstructed (a) MOF (EM, 24 iterations) and (b) NP (EM, 80 iterations) volumes.
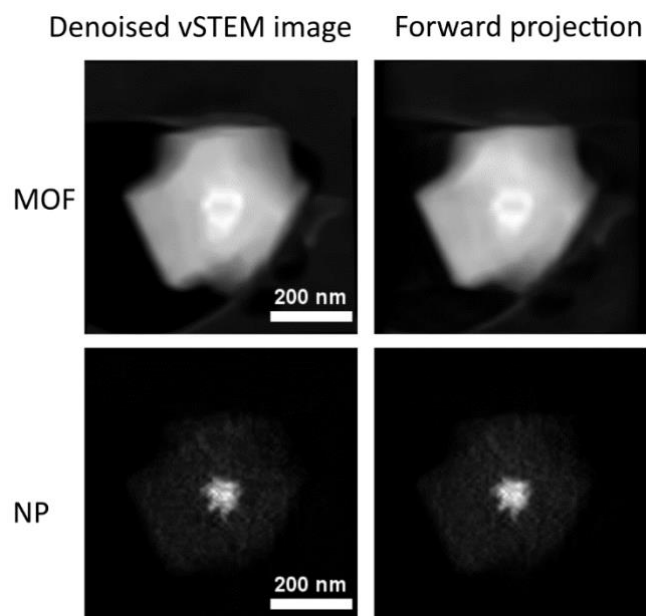
Figure S3: Exemplary denoised vSTEM images and forward projections from the reconstructed volume (MOF and NP) for -30° sample tilt.
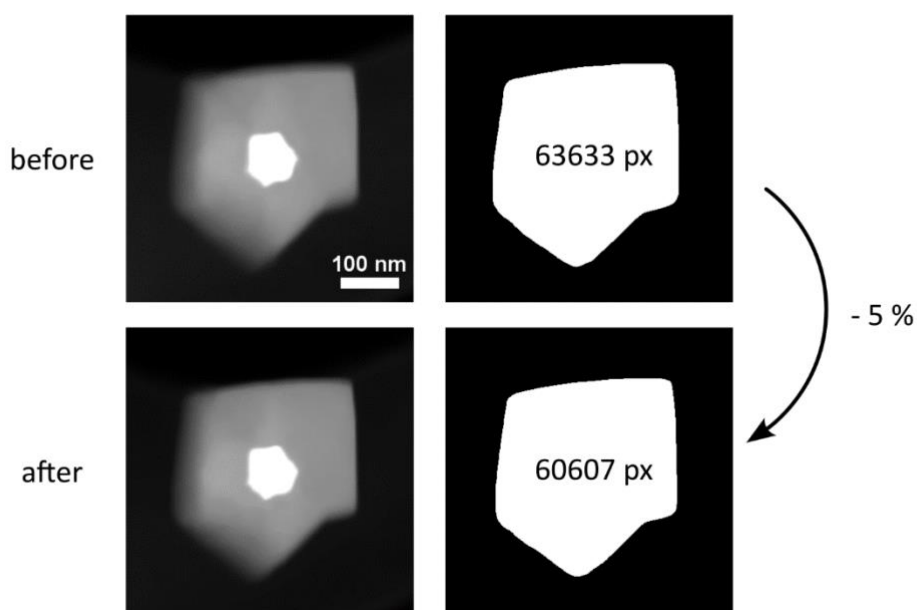

Figure S4: Evaluation of shrinkage during a fast tomography tilt series (including the dose spent for aligning the particle) using conventional STEM, by comparing the projected area of the particle at 0° before and after the tilt series.

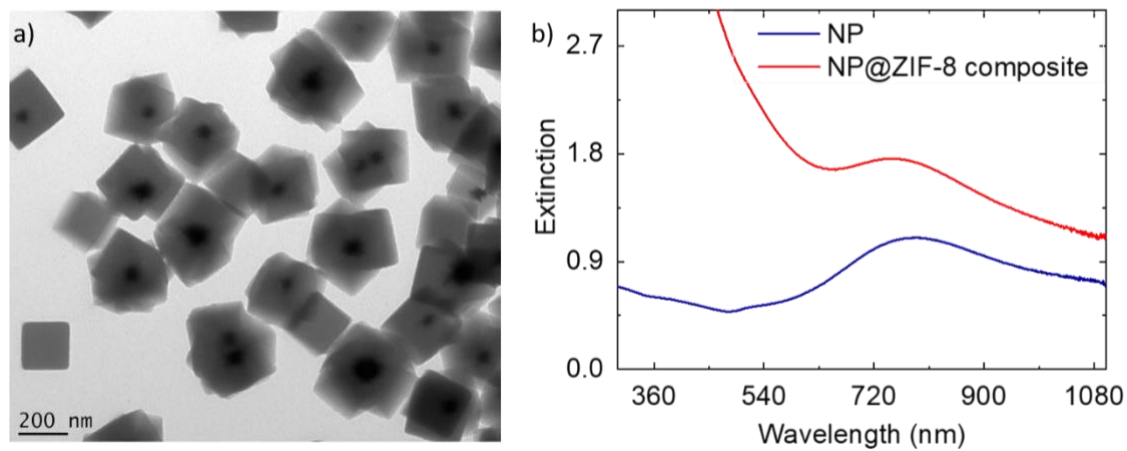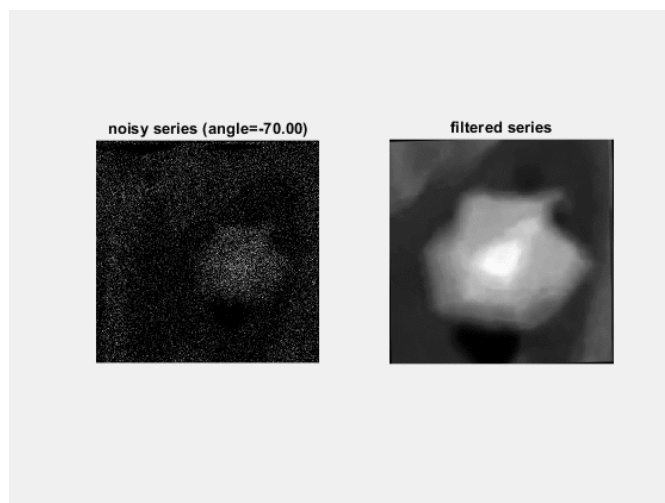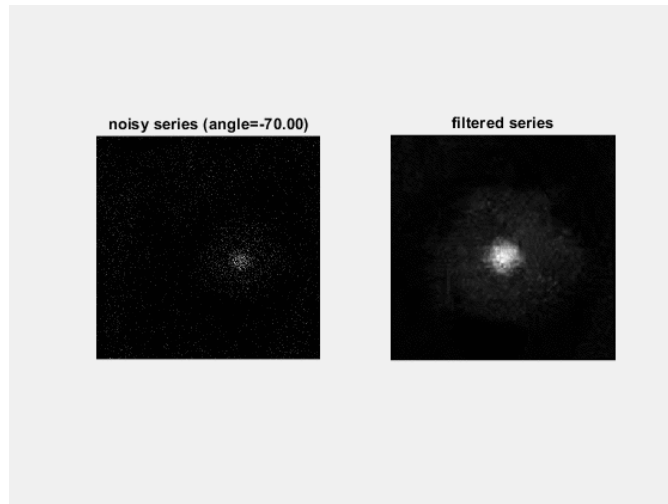**Low-resolution TEM image and UV-vis spectra of NP and NP@ZIF-8 composite**

Figure S5: a) Low-resolution TEM image of NP@ZIF-8 composite. b) Extinction spectra of NP and NP@ZIF-8 composite.

Original and denoised tilt series, video of the reconstructed volume

File 1: Original and denoised tilt series of the MOF

File 2: Original and denoised tilt series of the NP

File 3: Video of the 3D reconstruction

References

(1) Gu, S.; Timofte, R. A Brief Review of Image Denoising Algorithms and Beyond. In *Inpainting and Denoising Challenges*; Escalera, S., Ayache, S., Wan, J., Madadi, M., Güçlü, U., Baró, X., Eds.; The Springer Series on Challenges in Machine Learning; Springer International Publishing: Cham, 2019; pp 1–21. https://doi.org/10.1007/978-3-030-25614-2_1.

(2) Thanh, D.; Surya, P.; Hieu, L. M. A Review on CT and X-Ray Images Denoising Methods. *Informatica* **2019**, *43* (2).